



HAL
open science

Bending of the "9+2" axoneme analysed by the finite element method

Christian Cibert, Jérémy Toscano, Vincent Pensée, Guy Bonnet

► **To cite this version:**

Christian Cibert, Jérémy Toscano, Vincent Pensée, Guy Bonnet. Bending of the "9+2" axoneme analysed by the finite element method. *Journal of Theoretical Biology*, 2010, 264 (4), pp.1089-1101. 10.1016/j.jtbi.2010.03.040 . hal-00594151

HAL Id: hal-00594151

<https://hal.science/hal-00594151>

Submitted on 19 May 2011

HAL is a multi-disciplinary open access archive for the deposit and dissemination of scientific research documents, whether they are published or not. The documents may come from teaching and research institutions in France or abroad, or from public or private research centers.

L'archive ouverte pluridisciplinaire **HAL**, est destinée au dépôt et à la diffusion de documents scientifiques de niveau recherche, publiés ou non, émanant des établissements d'enseignement et de recherche français ou étrangers, des laboratoires publics ou privés.

Author's Accepted Manuscript

Bending of the "9+2" axoneme analysed by the finite element method

Christian Cibert, Jérémy Toscano, Vincent Pensée, Guy Bonnet

PII: S0022-5193(10)00175-X
DOI: doi:10.1016/j.jtbi.2010.03.040
Reference: YJTBI5941

To appear in: *Journal of Theoretical Biology*

Received date: 27 April 2009
Revised date: 26 March 2010
Accepted date: 29 March 2010

Cite this article as: Christian Cibert, Jérémy Toscano, Vincent Pensée and Guy Bonnet, Bending of the "9+2" axoneme analysed by the finite element method, *Journal of Theoretical Biology*, doi:10.1016/j.jtbi.2010.03.040

This is a PDF file of an unedited manuscript that has been accepted for publication. As a service to our customers we are providing this early version of the manuscript. The manuscript will undergo copyediting, typesetting, and review of the resulting galley proof before it is published in its final citable form. Please note that during the production process errors may be discovered which could affect the content, and all legal disclaimers that apply to the journal pertain.



www.elsevier.com/locate/jtbi

BENDING OF THE “9+2” AXONEME ANALYSED BY THE FINITE ELEMENT METHOD

Christian Cibert^{1,3}, Jérémy Toscano², Vincent Pensée² and Guy Bonnet²

Running title: Bending of the proximal segment axoneme.

¹-Er 3 “Biogenèse Des Signaux Peptidiques”, Université Paris VI, 2, place Jussieu, F-75252 Paris. Phone: 33 (0)6 77 13 46 71. Present address: Laboratoire d'Ingénierie des Systèmes de Versailles (LISV), Université de Versailles Saint-Quentin-en-Yvelines (UVSQ), 10/12, avenue de l'Europe, F-78140 Vélizy. E-mail: cibert@lisv.uvsq.fr

²- Université Paris-Est, Laboratoire de Modélisation et simulation multi-échelle, CNRS, FRE 3160, 5, bd. Descartes F-77454 Marne-la-Vallée, Cedex 2.

³- Author for correspondence.

Key words : axoneme, bending, finite element, flagellum, sliding.

ABSTRACT

Many data demonstrate that the regulation of the bending polarity of the “9+2” axoneme is supported by the curvature itself, making the internal constraints central in this process, adjusting either the physical characteristics of the machinery or the activity of the enzymes involved in different pathways. Among them, the very integrated Geometric Clutch model finds this regulation on the convenient adjustments of the probability of interaction between the dynein arms and the β -tubulin monomers of the outer doublet pairs on which they walk. Taking into consideration (i) the deviated bending of the outer doublets pairs (Cibert, C., and Heck, J.-V., (2004), *Cell Motil. Cytoskel.* **59**: 153-68), (ii) the internal tensions of the radial spokes and the tangential links (nexin links, dynein arms), (iii) a theoretical 5 μ m long proximal segment of the axoneme and (iv) the short proximal segment of the axoneme, we have reevaluated the adjustments of these intervals using a finite element approach. The movements we have calculated within the axonemal cylinder are consistent with the basic hypothesis that found the Geometric Clutch model, excepted that the axonemal side where the dynein arms are active increases the intervals between the two neighbor outer doublet pairs. This result allows us to propose a mechanism of bending reversion of the axoneme, involving the concerted ignition of the molecular engines along the two opposite sides of the axoneme delineated by the bending plane.

INTRODUCTION

Axoneme is the macromolecular scaffold that makes motile the flagella and cilia of the eukaryotic cell (Gibbons, 1981). From a physical point of view, it is a cylinder of nine longitudinal beams (the nine Outer Doublet Pairs of microtubules (ODPs)), which surrounds a central apparatus organized by two longitudinal beams (the central pair of microtubules (Downing and Sui, 2007; Sui and Downing, 2006)). The coordinated sliding of the ODPs (because of the activity of the periodical dynein arms (DA), the molecular motors (Burgess et al., 1991a; Burgess et al., 2003; Burgess et al., 1991b; Goedecke and

Elston, 2005; Hamasaki et al., 1995; Lindemann and Hunt, 2003; Mallik et al., 2004; Omoto et al., 1991; Shingyoji et al., 1998)) is converted to bending because of the presence of periodic elastic molecular links between each pair of ODPs (the nexin links (NL) and the dynein arms themselves) (Brokaw, 1989; Cibert, 2001; Downing and Sui, 2007; Lindemann, 1994b; Lindemann and Mitchell, 2007; Lindemann et al., 2005)), and the periodic radial spokes (RS), which link each ODP to the central apparatus (Cibert, 2003; Dymek and Smith, 2007; Gardner et al., 1994; Goodenough and Heuser, 1985; Lindemann, 2007; Mitchell et al., 2005; Mitchell and Nakatsugawa, 2004; Smith and Yang, 2004; Yang et al., 2001). This mechanism induces the propagation of a wave train along the organelles.

Instantaneous regulation of the machinery remains, however, mainly unknown, in spite of the existence of clever biochemical and topological models (Brokaw, 1975; Dymek and Smith, 2007; Gertsberg et al., 2004; Hayashi and Shingyoji, 2009; Huang et al., 1982; Inaba, 2003; Li et al., 2006; Lindemann, 1994a; Lindemann, 2007; Lindemann and Mitchell, 2007; Mitchell, 2003a; Mitchell, 2003b; Morita et al., 2006; Morita and Shingyoji, 2004; Noguchi et al., 2000; Noguchi et al., 2005; Piperno et al., 1992; Rupp and Porter, 2003; Smith and Yang, 2004; Wilson and Lefebvre, 2004; Woolley, 1997).

Among them, the Geometric Clutch (GC) model proposed by Lindemann assumes that the activity of the DAs along the two opposite faces of the axoneme depends on the inter-doublet interval that varies during the alternating beating movement: the larger the interval, the lower the canonical propulsive activity of the DAs (which is basically directed toward the minus end of the microtubules (Lindemann, 1994a)); this model promotes the role of the self-organization of the axoneme in the instantaneous regulation of its own machinery (Goldstein et al., 2008; Lindemann and Hunt, 2003; Lindemann, 2007; Sakakibara et al., 2004).

In this context, using a finite element approach (Cibert and Heck, 2004), we have studied the deformation of the proximal 5 μm long segment of a “9+2” axoneme to analyze what might be the topological events occurring at this level, accounting for the synchronous sliding hypothesis (Brokaw, 1996; Goldstein, 1976).

MODEL AND CALCULATION

We use the finite element method to calculate the deformed configurations of a theoretical model whose mechanical characteristics were assumed to be equivalent to that of a real axoneme. The calculus is performed using MSC NASTRAN, the “finite element” software used in the industrial field (MSC Software Corporation, USA). All parts of the model are linearly elastic, but nonlinear effects are taken into account: they come from the computation of second order moments induced when the actual configuration after displacement instead of the initial configuration is taken into account for computing internal moments.

Model meshing was done from the knowledge of the axonemal ultrastructure and the basic mechanisms that make it motile.

The first step of the modeling was dedicated to the definition of the bio-mechanical characteristics of the axonemal elements assumed to be essential in the axonemal movement (Figure 1 and Figure 2). We have considered two sorts of elements: beams (which transmit internal moments and longitudinal forces) and rods (which transmit longitudinal forces only). Elements modeled as rods are linked to beams by pin junctions. ODPs, dynein arms and central apparatus are modeled as beams. The other components of the axoneme (*i.e.* the nexin links, the radial spokes and the actuators) were modeled as rods.

Second, because of the longitudinal periodicities of the appendages carried by the ODPs (dynein arms, nexin links and radial spokes) and the cylindrical organization of the axoneme, model is constituted by a series of cylindrical 96 nm long modules, organized by the nine outer doublets associated each to 1 radial spoke, 1 nexin link, 1 outer dynein arm and 1 inner dynein arm, where each of these appendages are considered to be equivalent to the 3 radial spokes, the nexin link, the 4 outer dynein arms and the 3 inner dynein arms constitutively located along the homologous 96 nm long segment of the biological model (Figure 1 and Figure 2). The central apparatus of the axoneme is modeled as a beam along which the heads of the radial spokes are linked by pin junctions.

In the model, the dynein arms do not link directly nodes #3 and 5 of the ODP on which they are permanently bound as observed in the biological situation; they are carried by their actuators only (Figure 1 and Figure 2). This was the *sine qua non* condition to limit the artifactual bending of the model that we observed using a previous version of the model, considering dynein arms modeled each as a bar. When dynein arms are modeled as bar series along the ODPs, curvature of the model is opposite to that expected. The advantage of the conformation we have chosen is that it reduces the incidence of the forces which are tangential and normal to the axis of the model; in this model the ODPs can move within the axonemal cylinder and be active on the elasticity of both the DAs and the NLs.

The third step is the definition of the modes according to which the actuators of the dynein arms have to move along and around the model (Figure 1). Because of the synchronous sliding and the rigid anchoring of the ODPs at the proximal end of the biological model, the local shear — obtained at a given curvilinear abscissa — depends on the sum of the elementary shear involving each the modules located upstream and at this curvilinear abscissa. Consequently, to promote the bending of the model, we have chosen to move the two actuators associated to each of the dynein arms along the module series according to a linear gradient of amplitude. The activation of the upstream and downstream actuators of each dynein arm were produced using the concept of free deformations (Appendix 1) and according to a gradient along each of the ODPs to obtain a curvature that depends on the cumulative sliding (Appendix 2). Thus, we defined a linear gradient of free deformations along the model that increases and decreases of the same amplitude the length of the two actuators. To limit the skewing and twisting of the model, because of its basic cylindrical architecture, deformations of the actuators depend (at each curvilinear abscissa) on the lengths of the projections of the arms (IDA, ODA) on the bending plane, which has been considered to be constant along the entire length of the model (Cibert, 2002) (Appendix 3).

It is noteworthy that we have calculated only equilibriums. But, because the curvatures are low under our conditions, the intermediate conformations of the model that would exist between the straight conformation and the curved one could be deduced from the knowledge of these initial and final states.

RESULTS AND DISCUSSION

Internal loading of the axoneme was calculated under two pairs of basic modes (I, II, III and IV) (Figure 3), modifying the lengths of the actuators of the dynein arms as described above (Figure 1). Both of them induce the relative shear of the ODPs (Figure 4).

Under the loading modes I (+z), dynein arms located along the two opposites sides of the axoneme defined by the rank of the outer doublet [#6,7,8,9] and [#1,2,3,4] produce a force directed toward the minus end of the outer doublet on which they walk (their canonic activity) and are inactive, respectively. Along the inactive side of the axoneme, DAs are

simply absent; consequently the NLs and the RSs insure the cohesion of the axonemal cylinder and the distribution of the constraints inside the model along this side. Under the loading mode II (-z) the situation is inverted.

Under loading modes III (+z) and IV (-z), the DAs located on the two opposite sides of the axoneme pull and push on the neighboring ODPs to promote the bending of the model in the same polarity. These two loading modes are limit cases, because they imply that along one of the opposite sides of the axoneme, the dynein arms produce forces in the “anti canonic” direction (*i.e.* toward the plus end of the outer doublets on which they walk) a situation which was observed *in vitro*, studying reconstructed mammalian models (Lindemann and Hunt, 2003; Lorch et al., 2008). These four loading modes are defined to induce planar bends (Appendix 2 and Appendix 3). Our calculations neglect the incidence of the swimming medium because only the equilibrium — and not the steady state — of the movement is considered, even if it is clearly demonstrated that the swimming medium has a direct regulatory effect on the axonemal machinery (Brokaw, 1966a; Brokaw, 1966b; Cortez et al., 2004; Hilfinger and Jülicher, 2008).

Figure 6 shows the tangential forces of the RSs and the NLs. These diagrams allowed us to define the length of the segment of interest of the bent models we obtained under the 4 loading modes. Taking into consideration the tangential forces of the RSs, we observed that (i) they increase rapidly, (ii) their maximum range is observed closely to the 21st module and, (iii) after this abscissa, they converge, tending to 0 at the level of the 41st module. Along the 10 last modules, the graphs superpose and are difficult to be analyzed. Thus, we have chosen to consider the segments of interest constituted by the 41 proximal modules along the deformed models.

Figure 7 shows the deformations of the central apparatus that represent the 3D-bending of the model we have obtained under the four loading modes. In spite of the conditions we have chosen, which normally must induce planar bends, loading modes I and II induce clearly the 3D-bending, because projections of the curvature in the xy plane under these two loading modes have the same sign. This means that the effective bending planes we obtain when the model bends in the -z and +z direction form a dihedron. Under loading modes III and IV, curvatures of the model in the xy and the xz planes are roughly proportional, whatever the ranks of the module; the arcs obtained under these two loading modes are coplanar.

The observation of a curvature in the y direction is not expected, because, as stated above, the actuation of the dynein arms was defined in order to induce the bending in the xz plane only. This has to be considered however, more carefully. First, the absolute value of the ratio of the displacements observed in the two perpendicular planes xy and xz at the end of the segment of interest (Figure 7) equals $500/25 (\approx 20)$, $500/16 (\approx 30)$, $650/25 (\approx 25)$ and $650/27 (\approx 25)$ under the 4 loading modes, respectively, making the xy component lower than the xz one. Second, when the model is studied in a mathematical linear context (not shown), the projections of the arcs in the xy plane superpose on the x axis. This demonstrates that the nonlinear terms are incident in this calculation, even if they induce a secondary bending of short magnitude.

The movements of the ODPs occurring within the 21st module under the 4 loading modes are presented in Figure 8 and Figure 9. Loading modes I and II induce very symmetrical deformation in regard to both the cylindrical (Figure 8 left) and longitudinal (Figure 8 right) deformation of the model, because they generate pendulous movements of the ODPs that remain however, untwisted around their axis of inertia, in spite of their rotation around the axonemal cylinder. The most important observation is that, under these two loading modes

in which the dynein arms located along one side of the axoneme are inactive, intervals between the active ODPs increase while those of the inactive ODPs decrease. Loading modes III and IV, in which the two opposite sides are active (in two opposite directions), induce the increase of the intervals of the ODPs on the two opposite sides.

Figure 10 and Figure 11 describe the conformation of 41st cross section of the segment of interest observed under the 4 loading modes. Along these 20 distal elements, under the loading mode I and II, the intervals between active ODPs are always larger than those of ODPs located on the opposite inactive side of the axoneme, even if the axoneme is involved in a global twisting. Under the loading modes III and IV, the two opposite halves of the axoneme delineated by the bending plane, converge toward the inner side of the curvature, but the intervals between the ODPs located along the two active opposite side are always larger than the others.

Consequently, activity of the dynein arms along the ODPs induces the increase of the intervals of the ODPs, whatever the polarity of the force they produce.

Our calculations show also that, along the active side (whatever the polarity of the force it produces), the outer doublets are pushed–baseward; the outer doublets dynein arms of which are inactive are pulled tipward. The outer doublets located outside the curvature are pulled baseward.

From a biological point of view, the moments due to the relative displacements of nodes #1 and 4 — that create mechanical tensions inside the walls of the ODPs — associated to the flexions of the RSs that constrain node #4 as well as the central apparatus, could be involved in the regulation of the axonemal machinery via either the DRC (dynein regulatory complex), which are assumed to be involved in the direct regulation of the dynein arms in the actual biological system (Nakano et al., 2003; Rupp and Porter, 2003), or the tubulin monomers themselves — associated to the ensemble of the molecules that contribute to the architecture of the ODPs — since the calculations show that the distribution of these moments, their sign and their modules depend on the bending polarity and on the loading mode.

Because the orientations of the ODPs are constant during their rotation around the axonemal cylinder, the apparent lengths of the inner and of the outer dynein arms vary in such a way that those of the outer dynein arms are shortened as compared to those of the inner dynein arms (Cibert and Heck, 2004). This mechanism could be involved in the discrimination of the functions of the inner and outer rows of dynein arms (Brokaw, 1999). In effect, because of the rotation of the ODPs, the orientation of the bending plane has to change locally, and the activities of the two rows of dynein arms have to be adjusted as functions of these joint rotations.

As stated above the main results of this study is that the intervals of the ODPs whose dynein arms are active increase, while they decrease along the inactive side of the machinery, whatever the polarity of the walk of the dynein arms (Figure 6). They are consistent with the experimental observations that demonstrate the “respiration” of the axoneme (Lindemann and Mitchell, 2007; Sakakibara et al., 2004), (*i.e.* the local and cyclic variations of the diameter of the axoneme when it beats). They contradict, however, partly the hypotheses that found the Geometric Clutch model (Lindemann, 2007) because of the sign that characterizes the polarity of the relative displacements of the ODPs along the “active” and the “inactive” opposite sides of the axoneme.

Because the finite element method takes into consideration more than the longitudinal tensions (as proposed by the Geometric Clutch model), but the constraints due to the

deviated bending of the ODPs and the ones due to the radial spokes and the tangential links in regard to the axonemal cylinder (nexin links and dynein arms), this result is not surprising. The existence of ODP groups within the axonemal cylinder seems to be less significant on its own than the necessary adjustments of the relative intervals between the ODPs in which these groups are involved.

Comparison of the cylindrical deformations we observe under the four loading modes allows us to propose a scheme that could explain the reversion of the bending polarity of the axoneme, this mechanism being equivalent whatever the curvilinear abscissa along the model (Figure 12 and Figure 13). Assuming that: (i) interval between two neighboring ODPs increases when the dynein arms are active, (ii) loading modes I and II are the basic modes allowing the axoneme to bend, (iii) compressed inactive side becomes active during a short period of time inducing the “anti-canonic” polarity of the dynein arms movement, we propose that after the overflowing of internal tension, the activities of the opposite sides of the axoneme revert, and induce the change in the internal tension of the axoneme. In this scheme, the dynein regulatory complex (Piperno et al., 1992; Rupp and Porter, 2003) could play a crucial function, because it could be sensitive to the moments involving nodes #1 and 4 of each ODP that we have characterized along a 5 μm long segment of the axoneme.

We did not observe however, any displacement of the central pair toward the external side of the curvature as described in the case of the flagellum of *Chlamydomonas* (Mitchell, 2003b). Taking into consideration the assumptions we used, the central apparatus is modeled as a beam whose location within the axonemal cylinder depends on the constraints due to the radial spokes, which have been also modeled as beams. Consequently, the rigidity of our model could limit the actual displacement of the central apparatus within the axoneme, the more so as, *in vivo*, these displacements could involve passive and active mechanisms within the complex constituted by the spoke heads and the central apparatus, the last being impossible to conceive in the context of this study.

Topological adjustments are directly involved in the regulation of the axoneme as proposed by the geometric clutch model proposed by Lindemann, the “switch point” that drives the alternating shear of the ODPs (Satir and Matsuoka, 1989) could be considered as those that regulate the small-world networks because of the similitude that exists between the architecture of the axoneme and that of these networks (Barabasi and Albert, 1999; Barabasi and Bonabeau, 2003; Lahtinen et al., 2001; Newman, 2003; Newman and Watts, 1999; Newman et al., 2001; Newman et al., 2002).

TABLES AND FIGURE CAPTIONS

Table 1 **The mechanical characteristics of the rods appendages.** Rod elements. All rods have a full discoid cross section. The radius of the radial spokes and the nexin links equals 8 nm and 4 nm, respectively. The nexin links Young's modulus corresponds to a spring constant that equals $1.6 \cdot 10^{-5}$ pN.nm² (Lindemann, 2003). The section of the radial spokes is roughly four times the section of the nexin links, as observed on real sections. The Young's modulus of these elements has been taken as the one of the actuators. The tangential stiffness of the actuators of the dynein arms has been reduced in such way that they do not contribute significantly to the stiffness of the main part of the axoneme. We have checked the incidence of the forces transmitted by the actuators to the dynein arms, and we have verified that they do not induce the artifactual bending of the ODPs – under the construction conditions we have chosen – in spite of the lattice they constitute.

Table 2 **The mechanical characteristics of the beams appendages.** The beams that represent the ODPs have a full discoid cross section whose radius equals 8 nm. Their Young modulus and Poisson's ratio are taken from (Schoutens, 1994; Tuszyński et al., 2005); their flexure inertias are given by Schoutens, 1992 and Cibert and Heck, 2004. Young's modulus is that calculated by Schoutens, 1992. The shear coefficients (k_y and k_z) are obtained by considering a hollow cylinder. The area is obtained by considering a substructure of 23 protofilaments whose radius is 2.3 nm (Warner, 1976). The T-beams are those that link the nodes [1, 2], [1, 3], [1, 4] and [4, 5] within the periodic plateaus that mimic the cross section of the ODPs (figure 1). The central apparatus is modelled as a pair of beams of discoid cross section (microtubules) made of 13 protofilaments each (Warner, 1976). Its inertia moments are given by (Cibert and Heck, 2004). Beams modelling ODA and IDA have a full discoid cross section of 8 nm radius, but their moments of inertia have been enhanced by considering a hollow structure; this enforces a better transmission of the flexure moments to the ODP.

Figure 1: **The model.** **A:** within each section, each ODP was modeled as a series of 4 edges that link 5 nodes. Node #1 is the centre of inertia of the ODP. Node #2 is the centre of the incomplete microtubule (*B*), and represents the site towards which converge dynein arms carried by the neighboring ODP; the complete tubule is named *A*. Nodes #3 and 5 are the sites where the outer dynein arm (ODA) and the inner dynein arms (IDA) are permanently fixed, respectively. Node #4 is the site where the nexin link (NL) and the radial spoke (RS) are carried. Each of these appendages (excepted the NL whose spatial frequency equals $1/96$ nm⁻¹) represents the series of homologous appendages carried along the 96 nm long segment of each ODP of the actual axoneme. The actuators (red lines) of the dynein arms (green arrows) are bars submitted to free deformations. **B:** the lateral view of two parallel *N* and *N+1* ODPs (horizontal large grey bars), whose node #1 associates the rods [1-2] (lower vertical thin grey bar) and [1-[3-5]] (upper vertical thin grey bar); within the brackets the numbers are the ranks of the nodes that delineate each beam. The links of the actuators at both of their two ends are joints. The dynein arm is embedded in node #2 of the neighbor ODP. When the actuators *X* and *X+1* dilate and contract simultaneously because of the local adjustment of their free

deformations, the dynein arm produces a force applied on node #2 of the neighboring ODP. This force moves the ODP of rank N either in the canonical direction (toward the minus end of the ODP of rank $N+1$), or in the opposite direction (anti-canonical direction). The central apparatus to which converge the radial spokes is represented as a longitudinal beam. Because of the gradient of activity of the actuators of the dynein arms we have created, which respects the geometry of the axoneme (Cibert, 2002), planar bends as expected, the bending plane including the doublet #1 and the middle of the [5-6] pair. See movie: architecture.

Figure 2: **3D-scheme of the model. A:** front view of a module. By convention the first ODP is located on the upper side of the scheme and the ODPs are numbered clockwise from 1 to 9. The broad segments represent the beams that model the cross sections of the ODPs, and the thin lines correspond to the appendages that they carry (Figure 1). The central pair is modeled as a beam on which the radial spokes are embedded. The ranks of the nodes – included in open circles – superpose on the ODP #2. The model is viewed from base to tip. **B:** 3D view of the model. The basal anchor is located at the left side of the model. The boundary conditions at basal anchor are such that all nodes are clamped; the other tip is free. See movie: “architecture”.

Figure 3: **The four loading modes of the model.** The axoneme is viewed base to tip. Under the loading mode I and III (the curvature is positive) the dynein arms located along the outer doublets [#6-9] are active according to their canonical polarity, it means that they move the outer doublet of which they are appendages (their cargo) toward the minus end of the doublet that they use as a track. Under the loading mode II and IV (the curvature is negative) the situation is inverted. Under the loading mode I and III the dynein arms located along the opposite side are absolutely inactive (free) or active pushing their cargo toward the anticanonic direction (toward the plus end of their track), respectively. Under the loading mode II and IV the situation is inverted.

Figure 4: **Deformation and sliding.** $-Z$ bending when two opposite sides are active (loading mode IV). Because of the activity of the dynein arms, the sliding of the ODPs is effectively responsible of the bending of the model. Color encoding: central apparatus (black), outer doublets, nexin links and outer dynein arms (and their actuators) (blue), inner dynein arms (and their actuators) (yellow), radial spokes (red).

Figure 5: **Method of analysis of the deformation of the bent model. (Left side).** As shown in Figure 2, the cross section corresponds to the tipward view of the model, and the numbers included inside the tubule-A indicate the rank of the ODPs. By convention, these numbers are blue and white when the dynein arms are inactive and active, respectively. The white numbers are associated to a sign $-$ or $+$ when the arms move in the “canonic direction” (baseward) and the “anti-canonic direction” (tipward) the ODP on which they are associated permanently (their cargo). The blue background of each of the ODPs defines the cylindrical location and the orientation of each of them within the embedded first cross section of the model. The thin blue and white lines, which are parallel to the orientations of the ODPs, represent the orientations of the ODPs calculated at the level of the basal anchor and within a given cross section, respectively. The angle between these lines defines the twist of

the ODPs. In this scheme, the lines that superpose on the outer and inner dynein arms carried by the ODPs are the 2D-Euclidean distances between nodes #3 and #5 and the surfaces of the neighboring ODP; they are homologous to the intervals that can be measured on electron microscope pictures, assumed to be incident in the regulation of the dynein arms as proposed in the GC model. The colors of the arms range within the scale designed by the vertical linear gradient, and characterize the capability of the dynein arms to grasp a β -tubulin monomer, assuming that the shortest their length, the highest the activity of the arms (as proposed by Lindemann, 1994), the brightest the arm. The other appendages carried by the ODPs (the nexin links (NL) and the radial spokes (RS)) are schematized using the same color encoding that corresponds here to their 3D-lengths, which are consistent with the tangential forces that subject them; the shortest a link, the brightest the color. The rank of the ODPs that carry the NLs and the RSs are written on the left and the right side of the vertical color scale, respectively. In the upper left corner of the image the expected polarity of bending (+z, -z) is indicated. **(Right side)** The longitudinal deformation of the model is characterized by the side view of the cross section designed on the right side of the model. In this scheme, nodes #1 and #4 as well as their links and the radial spokes are represented according to a same color scale as that described above but that corresponds here to their ordinate (y) only (Figure 2). Nodes #1 are the outer ones. By convention, the basal anchor is located on the right side of the scheme. Thus, ODP #8 is the brightest being located in the front plane. The number written at the left side of “basal anchor” in the upper right corner of the image is the magnification coefficient of the longitudinal deformation of the cross section (x axis), which depends on the loading mode; this value was determined — for design reasons only — in such a way that the maximum of the longitudinal displacements of the nodes calculated under the four loading modes equals the half of the diameter of the model.

Figure 6: **Tangential forces within the radial spokes and the nexin links.** The color encoding of the curves, that corresponds each to a given ODP, is shown within the inset describing the tangential forces within the radial spokes that we obtained under loading mode I. The positive and negative values correspond to the dilation and the compression of the link, respectively. The tangential forces constraining the RSs under the 4 loading modes (as well as the NLs) are represented on the same range.

Figure 7: **xy and xz deformations of the segment of interest under the 4 loading modes I, II, III and IV.**

Figure 8: **The behavior of the 21st cross-section under loading modes I and II** (see movies loading_mode_I.avi and loading_mode_II.avi). Under loading mode I, ODP #1 remains immotile, the rotation of the other ODPs occurring counterclockwise; the larger displacement is that of ODP #5. Under loading mode II, the same counterclockwise rotation is observed, while the bending polarity is inverted, the outer doublet #6 and #2 being immotile and the most motile, respectively. ODP #5 moves in the clockwise direction. Correlatively to these global movements, the most important observation concerns the variations of the distances between neighboring ODPs, which are dilated and compressed along the active and the inactive opposite sides of the axoneme, respectively. The movements of the ODPs increase the diameter of the

axoneme included in the bending plane, and compress the model in the perpendicular plane. The lateral views of the axoneme at the same abscissa, confirm the symmetrical changes induced by the two loading modes I and II, and show that the longitudinal displacements of nodes #1 and #4 are not equivalent. As expected, because of the bending polarity, nodes #4 of the ODPs located on the inner and the outer sides of the curved segment are pushed tipward and pulled baseward, respectively; nodes #1 resting close to the vertical yz plane. The apparent neutral surface that includes ODPs #4 and 8 delineates the inner and the outer side of the curvature. These displacements create twisting moments inside the ODPs. The axes of these moments are roughly orthogonal to the bending plane.

Figure 9: **The behavior of the 21st cross-section under loading modes III and IV** (see movies `loading_mode_III.avi` and `loading_mode_IV.avi`). Under loading mode III, neighboring ODPs #1 and #9 appear to be immotile because they oscillate — with a low amplitude — around their basic position, and the other ODPs could be associated in three groups. ODPs #8, 7 and 6 on one hand, and ODPs #4 and 5 on the other hand, converge toward the outer side of the curvature (*i.e.* the 5-6 interval); these two groups are involved in a counterclockwise and a clockwise movement, respectively. ODPs #2 and 3 rotate counterclockwise and converge toward the inner side of the curvature. These movements define 4 sectors inside the cross section of the axoneme, delineated each by the expected bending plane (xz) and by the perpendicular direction that includes the neutral surface of the axoneme. Under loading mode IV, ODPs #1, 4 and 8 appear as immotile, and we observe the same movements of convergence of the other ODPs as those occurring under loading mode II in spite of the change of the bending polarity. These convergent rotations correspond to the net increase of the distance of the ODPs involved in both opposite active sides (whatever the polarity of the movement of the dynein arms). These movements enlarge the diameter of the axoneme included into the bending plane and compress the model in the perpendicular direction, as observed under loading modes I and II. As for the deformation of the side view of the model, the observations are the same as those described for the model constrained under loading modes I and II (Figure 8).

Figure 10: **The behavior of the 41st cross-section under loading modes I and II** (see movies `loading_mode_I.avi` and `loading_mode_II.avi`). Loading mode I and II induce a clockwise rotation of the ensemble of the ODPs and an adjustment of the intervals between neighboring ODPs, which (excepted one), shorten; the intervals between ODPs #1 and 2 (under loading mode I) and #5 and 6 (under loading mode II) increase. The intervals between active ODPs are always larger than those of ODPs located on the opposite inactive side. It is noteworthy that, even if the cylindrical rotation of the ODPs along the distal segment is opposite to that involving the 21 proximal modules, the superposition between the cylindrical location of each ODP and its location at the level of the basal anchor, never occurs. The side views of the model constrained by loading modes I and II show an amplification of the relative displacements of node #1 and 4, and that the active and the inactive sides of the model are respectively pushed tipward and pulled baseward in a symmetrical way. The apparent

neutral surface that includes ODPs #4 and 8 delineates the inner and the outer side of the curvature.

Figure 11: **The behavior of the 41st cross-section under loading modes III and IV** (see movies `loading_mode_III.avi` and `loading_mode_IV.avi`). Under these two loading modes the two opposite halves of the axoneme delineated by the bending plane — which are both active and promote the bending of the model in the same direction — converge toward the inner side of the curvature. At the end of the models, since the cylindrical locations of the ODPs are close to those they have within the first embedded cross section, the amplitude of the movement of each ODP is proportional to its displacement observed in the 21st cross section. This merge is never observed along the 20 modules that constitute the distal portion of the segment of interest, when the model is submitted to loading modes I and II, because the relative displacements of the ODPs within the axonemal cylinder are not synchronized. Intervals measured between the active ODPs located within the neutral surface — the plan orthogonal to the bending plane — are always larger than those of both couples of ODPs #1-2 and #5-6, which are located in the bending plane. As shown by the sides views, the longitudinal displacements of nodes #1 and 4 occurring along the distal part of the segment of interest could be considered as solely amplified as compared to those characterized at the level of the 21st cross section, excepted that nodes of ODPs #3, 4 and 8 are gently pulled toward the basal anchor.

Figure 12: **Bending and bending reversion at the 21st section.** The four insets are arranged vertically as a function of the bending amplitude (in the z direction) induced by each of the four loading modes. The color encoding is that described in Figure 5.

Figure 13: **Bending and bending reversion at the 41st section** (see text and **Figure 12**).

BIBLIOGRAPHY

- Badoual, M., Julicher, F., and Prost, J., 2002. Bidirectional cooperative motion of molecular motors. *Proc Natl Acad Sci U S A* 99, 6696-701.
- Barabasi, A.L., and Albert, R., 1999. Emergence of scaling in random networks. *Science* 286, 509-12.
- Barabasi, A.L., and Bonabeau, E., 2003. Scale-free networks. *Sci Am* 288, 60-9.
- Brokaw, C., 1999. Computer simulation of flagellar movement: VII. Conventional but functionally different cross-bridge models for inner and outer arm dyneins can explain the effects of outer arm dynein removal. *Cell Motility and the Cytoskeleton* 42, 134-48.
- Brokaw, C.J., 1966a. Effects of increased viscosity on the movements of some invertebrate spermatozoa. *J Exp Biol* 45, 113-39.
- Brokaw, C.J., 1966b. Mechanics and energetics of cilia. *Am Rev Respir Dis* 93, Suppl:32-40.
- Brokaw, C.J., 1975. Effects of viscosity and ATP concentration on the movement of reactivated sea-urchin sperm flagella. *J Exp Biol* 62, 701-19.
- Brokaw, C.J., 1989. Direct measurements of sliding between outer doublet microtubules in swimming sperm flagella. *Science* 243, 1593-6.
- Brokaw, C.J., 1996. Microtubule sliding, bend initiation, and bend propagation parameters of *Ciona* sperm flagella altered by viscous load. *Cell Motil Cytoskeleton* 33, 6-21.
- Bui, K.H., Sakakibara, H., Movassagh, T., Oiwa, K., and Ishikawa, T., 2008. Molecular architecture of inner dynein arms in situ in *Chlamydomonas reinhardtii* flagellum. *J. Cell Biol.* 183, 923-32.
- Burgess, S., and Knight, P., 2004. Is the dynein motor a winch? *Curr. Opin. Struct. Biol.* 14, 138-46.
- Burgess, S., Carter, D., Dover, S., and Woolley, D., 1991a. The inner dynein arm complex: compatible images from freeze-etch and thin section methods of microscopy. *J. Cell Science* 100, 319-28.
- Burgess, S., Walker, M., Sakakibara, H., and Oiwa, K., 2003. Dynein structure and power stroke. *Nature* 421, 715-8.
- Burgess, S.A., Dover, S.D., and Wooley, D.M., 1991b. Architecture of the outer arm dynein ATPase in an avian sperm flagellum, with further evidence of the B-link. *J. Cell Sci.* 98, 17-26.
- Carter, A.P., Garbarino, J.E., Wilson-Kubalek, E.M., Shipley, W.E., Cho, C., Milligan, R.A., Vale, R.D., and Gibbons, I.R., 2008. Structure and functional role of dynein's microtubule-binding domain. *Science* 322, 1691-5.
- Cibert, C., 2001. Elastic extension and jump of the flagellar nexin links: a theoretical mechanical cycle. *Cell Motil. Cytoskel.* 49, 161-75.
- Cibert, C., 2002. Axonemal activity relative to the 2D/3D-waveform conversion of the flagellum. *Cell Motility and the Cytoskeleton* 51, 89-111.
- Cibert, C., 2003. Entropy and information in flagellar axoneme cybernetics : a radial spokes integrative function. *Cell motility and the Cytoskeleton* 54, 296-316.
- Cibert, C., and Heck, J.V., 2004. Geometry drives the "deviated-bending" of the bi-tubular structures of the 9 + 2 axoneme in the flagellum. *Cell Motil Cytoskeleton* 59, 153-68.
- Cortez, R., Cowen, N., Dillon, R., and Fauci, L., 2004. Simulation of swimming organisms: coupling internal mechanics with external fluid dynamics. *Computing in sciences and engineering* 6, 38-45.
- Downing, K.H., and Sui, H., 2007. Structural insights into microtubule doublet interactions in axoneme. *C. O. S. B.* 17, 253-9.

- Dymek, E.E., and Smith, E., 2007. A conserved CaM- and radial spoke-associated complex mediates regulation of flagellar dynein activity. *J. Cell Biol.* 179, 515-26.
- Gardner, L., O'Toole, E., Perrone, A., Giddings, T., and Porter, M., 1994. Components of a "dynein regulatory complex" are located at the junction between the radial spokes and the dynein arms in *Chlamydomonas* flagella. *J. Cell Biol.* 127, 1311-35.
- Gennerich, A., Carter, A., Reck-Peterson, S., and Vale, R., 2007. Force-induced bidirectional stepping of cytoplasmic dynein. *Cell* 131, 952-65.
- Gertsberg, I., Hellman, V., Fainshtein, M., Weil, S., Silberberg, S.D., Danilenko, M., and Priel, Z., 2004. Intracellular Ca²⁺ regulates the phosphorylation and the dephosphorylation of ciliary proteins via the NO pathway. *J Gen Physiol* 124, 527-40.
- Gibbons, I.R., 1981. Cilia and flagella of eukaryotes. *J. Cell Biol.* 91, 1071-1245.
- Goedecke, D.M., and Elston, T.C., 2005. A model for the oscillatory motion of single dynein molecules. *J Theor Biol* 232, 27-39.
- Goldstein, B.N., Aksirov, A.M., and Zakrjevskaya, D.T., 2008. Kinetic model for dynein ascillation activity. *Biophysical Chemistry* 134, 20-4.
- Goldstein, S., 1976. Form of developing bends in reactivated sperm flagella. *J. Exp. Biol* 64, 173-84.
- Goodenough, U., and Heuser, J., 1985. Substructure of inner dynein arms, radial spokes, and the central pair/projection complex of cilia and flagella. *J. Cell Biol.* 100, 2008-18.
- Hamasaki, T., Holwill, M.E., Barkalow, K., and Satir, P., 1995. Mechanochemical aspects of axonemal dynein activity studied by in vitro microtubule translocation. *Biophys J* 69, 2569-79.
- Hayashi, S., and Shingyoji, C., 2009. Bending-induced switching of dynein activity in elastase-treated axonemes of sea urchin sperm, roles of Ca²⁺ and ADP. *Cell Motil Cytoskeleton* 66, 292-301.
- Hilfinger, A., and Jülicher, F., 2008. The chirality of ciliary beats. *Phys. Biol.* 5, 1-12.
- Huang, B., Ramanis, Z., and Luck, D.J.L., 1982. Suppressor mutation in *Chlamydomonas* reveals a regulatory mechanism of flagellar function. *Cell* 28, 115-124.
- Inaba, K., 2003. Molecular architecture of the sperm flagella: molecules for motility and signaling. *Zoolog. Sci.* 20, 1043-56.
- Ishikawa, T., Sakakibara, H., and Oiwa, K., 2007. The architecture of outer dynein arms in situ. *J. Mol. Biol.* 368, 1249-58.
- Lahtinen, J., Kertesz, J., and Kaski, K., 2001. Scaling of random spreading in small world networks. *Phys Rev E Stat Nonlin Soft Matter Phys* 64, 057105.
- Li, C., Ru, C.Q., and Mioduchowski, A., 2006. Torsion of the central pair microtubules in eukaryotic flagella due to bending-driven lateral buckling. *B.B.R.C.* 351, 159-64.
- Lindemann, C., 1994a. A "geometric clutch" hypothesis to explain oscillations of the axoneme of cilia and flagella. *Journal of Theoretical Biology* 168, 175-89.
- Lindemann, C., 2003. Structural-functional relationships of the dynein, spokes, and central-pair projections predicted from an analysis of the forces acting within a flagellum. *Biophysical Journal* 84, 4115-26.
- Lindemann, C., and Hunt, A., 2003. Does axonemal dynein push, pull or oscillate ? *Cell Motility and the Cytoskeleton* 56, 237-44.
- Lindemann, C.B., 1994b. A model of flagellar and ciliary functioning which uses the forces transverse to the axoneme as the regulator of dynein activation. *Cell Mot. Cytoskel.* 29, 141-54.
- Lindemann, C.B., 2007. The Geometric Clutch as a working hypothesis for future research on cilia and flagella. *Ann N Y Acad Sci*, 477-93.

- Lindemann, C.B., and Mitchell, D.R., 2007. Evidence for axonemal distortion during the flagellar beat of *Chlamydomonas*. *Cell Motil Cytoskeleton* 64, 580-9.
- Lindemann, C.B., Macauley, L.J., and Lesich, K.A., 2005. The counterbend phenomenon in dynein-disabled rat sperm flagella and what it reveals about the interdoublt elasticity. *Biophys J* 89, 1165-74.
- Lorch, D.P., Lindemann, C., and Hunt, A., 2008. The motor activity of mammalian axonemal dynein studied in situ on doublet microtubules. *Cell Motil Cytoskeleton* 65, 487-94.
- Mallik, R., Carter, B.C., Lex, S.A., King, S.J., and Gross, S.P., 2004. Cytoplasmic dynein functions as a gear in response to load. *Nature* 427, 649-52.
- Mitchell, B.F., Pedersen, L.B., Feely, M., Rosenbaum, J.L., and Mitchell, D.R., 2005. ATP Production in *Chlamydomonas reinhardtii* Flagella by Glycolytic Enzymes. *Mol Biol Cell*.
- Mitchell, D., 2003a. Reconstruction of the projection periodicity and surface architecture of the flagellar central pair complex. *Cell motility and the Cytoskeleton* 55, 188-99.
- Mitchell, D.R., 2003b. Orientation of the central pair complex during flagellar bend formation in *Chlamydomonas*. *Cell Motil Cytoskeleton* 56, 120-9.
- Mitchell, D.R., and Nakatsugawa, M., 2004. Bend propagation drives central pair rotation in *Chlamydomonas reinhardtii* flagella. *J Cell Biol* 166, 709-15.
- Morita, M., Takemura, A., Nakajima, A., and Okuno, M., 2006. Microtubule sliding movement in tilapia sperm flagella axoneme is regulated by Ca(2+)/calmodulin-dependent protein phosphorylation. *Cell Motil Cytoskeleton* 63, 459-70.
- Morita, Y., and Shingyoji, C., 2004. Effects of imposed bending on microtubule sliding in sperm flagella. *Curr Biol* 14, 2113-8.
- Nakano, I., Kobayashi, T., Yoshimura, M., and Shingyoji, C., 2003. Central-pair-linked regulation of microtubule sliding by calcium in flagellar axonemes. *J Cell Sci* 116, 1627-36.
- Newman, M.E., 2003. The structure and function of complex networks. *SIAM Review* 45, 167-256.
- Newman, M.E., and Watts, D.J., 1999. Scaling and percolation in the small-world network model. *Phys Rev E Stat Phys Plasmas Fluids Relat Interdiscip Topics* 60, 7332-42.
- Newman, M.E., Strogatz, S.H., and Watts, D.J., 2001. Random graphs with arbitrary degree distributions and their applications. *Phys Rev E Stat Nonlin Soft Matter Phys* 64, 026118.
- Newman, M.E., Watts, D.J., and Strogatz, S.H., 2002. Random graph models of social networks. *Proc Natl Acad Sci U S A* 99 Suppl 1, 2566-72.
- Noguchi, M., Ogawa, T., and Taneyama, T., 2000. Control of ciliary orientation through cAMP-dependent phosphorylation of axonemal proteins in *Paramecium caudatum*. *Cell Motility and the Cytoskeleton* 45, 263-71.
- Noguchi, M., Kitani, T., Ogawa, T., Inoue, H., and Kamachi, H., 2005. Augmented ciliary reorientation response and cAMP-dependent protein phosphorylation induced by glycerol in triton-extracted *Paramecium*. *Zoolog Sci* 22, 41-8.
- Omoto, C., Palmer, J., and Moody, M., 1991. Cooperativity, in axonemal motion : analysis of a four-state, two-site kinetic model. *Proc. Natl. Acad. Sci. USA* 88, 5562-66.
- Piperno, G., Mead, K., and Shestak, W., 1992. The Inner Dynein Arms I2 Interact with a "Dynein Regulatory Complex" in *Chlamydomonas* Flagella. *J. Cell Biol.* 118, 1455-63.
- Roberts, A.J., Numata, N., Walker, M.L., Kato, Y.S., Malkova, B., Kon, T., Ohkura, R., Arisaka, F., Knight, P.J., Sutoh, K., and Burgess, S.A., 2009. AAA+ Ring and linker swing mechanism in the dynein motor. *Cell* 136, 485-95.

- Ross, J.L., Wallace, K., Shuman, H., Goldman, Y.E., and Holzbaur, E.L., 2006. Processive bidirectional motion of dynein-dynactin complexes in vitro. *Nat Cell Biol* 8, 562-70.
- Rupp, G., and Porter, M., 2003. A subunit of the dynein regulatory complex in *Chlamydomonas* is a homologue of a growth arrest-specific gene product. *J. Cell Biol.* 162, 47-57.
- Sakakibara, H., Kunioka, Y., Yamada, T., and Kamimura, S., 2004. Diameter oscillation of axonemes in sea-urchin sperm flagella. *Biophysical Journal* 86, 346-52.
- Satir, P., and Matsuoka, T., 1989. Splitting the ciliary axoneme implications for a 'switch-point' model of dynein arm activity in ciliary motion. *Cell Mot. & Cytoskel.* 14, 345-358.
- Schoutens, J., 1994. Prediction of elastic properties of sperm flagella. *Journal of theoretical biology* 171, 163-77.
- Shingyoji, C., Higuchi, H., Yoshimura, M., katayama, R., and Yanagida, T., 1998. Dynein arms are oscillating force generators. *Nature* 293, 711-14.
- Smith, E., and Yang, P., 2004. The radial spokes and central apparatus : Mechano-chemical transducers that regulate flagellar motility. *Cell Motil. Cytoskeleton* 57, 8-17.
- Sui, H., and Downing, K.H., 2006. Molecular architecture of axonemal microtubule doublets revealed by cryo-electron tomography. *Nature* 442, 475-8.
- Tuszynski, J.A., Luchko, T., Portet, S., and Dixon, J.M., 2005. Anisotropic elastic properties of microtubules. *Eur. Phys. J E Soft Matter* 17, 29-35.
- Ueno, H., Yasunaga, T., Shingyoji, C., and Hirose, K., 2008. Dynein pulls microtubules without rotating its stalk. *Proc Natl Acad Sci U S A* 105, 19702-7.
- Warner, F., Cross-bridge mechanism in ciliary motility: the sliding-bending conversion, in: Goldman, R., et al., Eds.), *Cell Motility (Part C)*, Cold Spring Harbor Laboratory 1976, pp. 891-914.
- Wilson, N.F., and Lefebvre, P.A., 2004. Regulation of flagellar assembly by glycogen synthase kinase 3 in *Chlamydomonas reinhardtii*. *Eukaryot Cell* 3, 1307-19.
- Woolley, D.M., 1997. Studies on the eel sperm flagellum. I. The structure of the inner dynein arm complex. *Journal of Cell Science* 110, 85-94.
- Yang, P., Diener, D., Rosenbaum, J., and Sale, W., 2001. Localization of calmodulin and dynein light chain LC8 in flagellar radial spokes. *J. Cell Biol.* 153, 1315-25.

Appendix 1

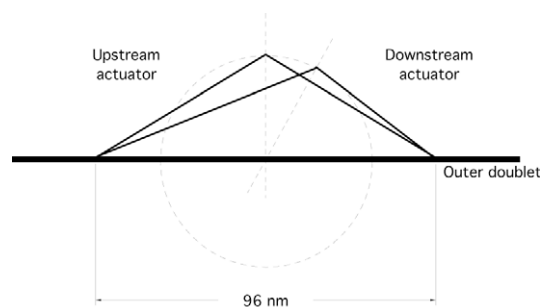
Modeling the effect of actuators using free deformations

The forces related to the effect of actuators must be self-equilibrated. This can be achieved by using the concept of free deformations. Consider a beam submitted to an increase in temperature δT . Under free conditions (*i.e.* without external constraints) beam would deform freely, and the equation: $\varepsilon^* = \alpha \delta T$, where ε^* is the free deformation, α is the dilation coefficient and T is temperature, describe the dilation effect. When the beam is submitted to a longitudinal constraint, free deformation is limited, and beam is submitted to a complementary elastic deformation due to this constraint (ε_e). This leads to the complete deformation ε given by the equation: $\varepsilon = \varepsilon_e + \varepsilon^*$. When the beam is clamped at both ends, the longitudinal deformation equals zero. Consequently, the longitudinal elastic deformation has to be exactly opposite to the free deformation ($\varepsilon_e = -\varepsilon^*$). It could be demonstrated that free deformations are equivalent to body forces, these body forces being always in equilibrium. In our model, free deformations were chosen to reproduce at best the biological movement of dynein arms, which is mediated by two “free deforming” rods (the actuators). When actuators dilate and contract in a coordinated manner along the entire length of the model, the whole scaffold deforms elastically in order to recover the internal equilibrium and the kinematical conditions at the boundaries.

Appendix 2

Coordinated variation in length of the two actuators of each dynein arm

Because the actuators of the dynein arms constitute a lattice associated to each outer doublet and contribute consequently to their inertia parallel to the major axis of their cross section, the mutual deformation of the upstream and downstream actuators which model the stem of the arm was calculated in such a way that the displacement of the nodes where they link the beam — which constitute the stalk/tether of the arm — does not induce on its own any artifactual curvature of the outer doublet.



To respect this condition, this node has to move along the dashed circle whose center is the middle of the 96 nm long segment of the outer doublet. This makes free deformation of the two actuators co-coordinated, avoiding internal tension in the triangle they constitute with the segment of the outer doublet. Practically, variation in length of one of the two-actuators was defined as a function of the local free deformation and of the position of the node around the axonemal cylinder; the variation in length of the second actuator was deduced from this calculation using geometry. The same method is used whatever the polarity of the force produced by the arm.

Recent publications demonstrate that the forces produced by the dynein arms seems to be due to a “winch” mechanism that involves the linker domain and the stem/tail of the arms, in place of the tilt of the stalk/tether, even if stalk/tether can tilt to regulate the size of the walking step of the arm, being more rigid than previously reported (Burgess and Knight, 2004; Carter et al., 2008; Roberts et al., 2009; Ueno et al., 2008). The stem/tail domain and the linked domain are assumed to play a major function because they are close to the AAA1 ATPase active site of the Walker ensemble. In this mechanism, the orientation of the force produced by the arm is either only parallel to the microtubule, when the AAA domain glides on the surface of the microtubule (as proposed by Ueno et al.), or oblique in regard to the orientation of the microtubules (as proposed by Carter et al.). It is noteworthy that these mechanisms are proposed from the study of either reconstructed systems or isolated arms, and that architecture of the axoneme makes the dynein arms of both the inner and outer rows interacting very closely (Bui et al., 2008; Ishikawa et al., 2007). So the actual mechanism according to which the forces are produced along and around the outer doublet pairs along and around the axoneme remains mainly speculative. We have chosen to construct the inner and outer dynein arms according to the same model described in Figure 1 and Figure 2, assuming that inner and outer of arms are able to produce forces having the same amplitude in the two polarities (*i.e.* toward the + and the – end of the outer doublets) (Badoual et al., 2002; Gennerich et al., 2007; Lindemann and Hunt, 2003; Ross et al., 2006) in a synchronous manner. Because of the small amplitude of the shear we have calculated, dynein arms are unable to jump and remain linked onto the wall of the doublet N+1. The scaffold we have constructed looks like the model proposed by Ueno et al. insofar as stalk/tether of each arm we have constructed is embedded in the wall of the

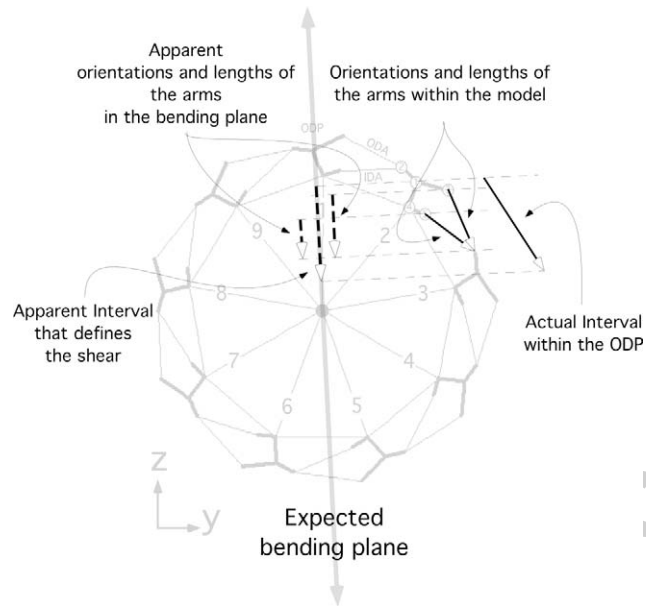
outer doublet $N+1$ (and does not tilt by default to produce a force), and the ensemble of actuators of each arm pushes and pulls the stalk/tether in a direction parallel to that of the two outer doublets linked by the stalk/tether they move.

Accepted manuscript

Appendix 3

Projection of the dynein arms one the bending plane

Because of the cylindrical organization of the axoneme, deformation of the dynein arms (IDA and ODA) was a function of their length of their projection on the expected bending plane.



From this scheme, the coefficients of correction of the relative activities of the IDA and the ODA were calculated to allow the planar bend of the model. In the following plot, plain and dashed curves represent the coefficients calculated for the IDA and the ODA, respectively.

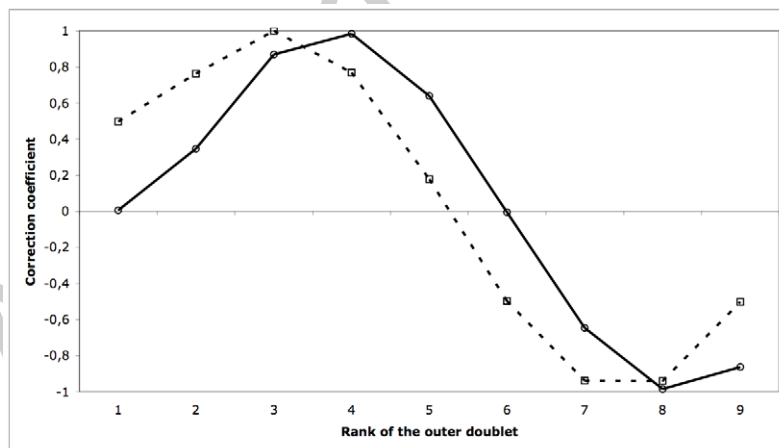


Table 1

	Nexin Links	Radial Spokes	Actuators of the dynein arms
E (pN.nm ²)	0.016	16	16
N	0.3	0.3	0.3
S (nm ²)	50	200	4
J (nm ⁴)	400	6,400	6,400

Accepted manuscript

Table 2

	Unit	ODP	T-beam	ODA IDA	Central Apparatus
Young's Modulus	E (pN.nm ²)	$2.0 \cdot 10^3$	$2.0 \cdot 10^3$	0.5	1.6
Poisson's ratio		0.3	0.3	0.3	0.3
Section	S (nm ²)	380	200	200	430
Flexure Inertias	{ I _y (nm ⁴)	$3.5 \cdot 10^4$	$3.2 \cdot 10^3$	$3.2 \cdot 10^3$	$7 \cdot 10^4$
		I _z (nm ⁴)	$5.3 \cdot 10^4$	$3.2 \cdot 10^3$	$3.2 \cdot 10^3$
Torsion inertia	J (nm ⁴)	$8.9 \cdot 10^4$	$6.4 \cdot 10^3$	$6.4 \cdot 10^3$	$30 \cdot 10^4$
Shear coefficients	{ k _y	0.5	0.9	0.9	0.5
		k _z	0.5	0.9	0.9

Accepted manuscript

Figure 1

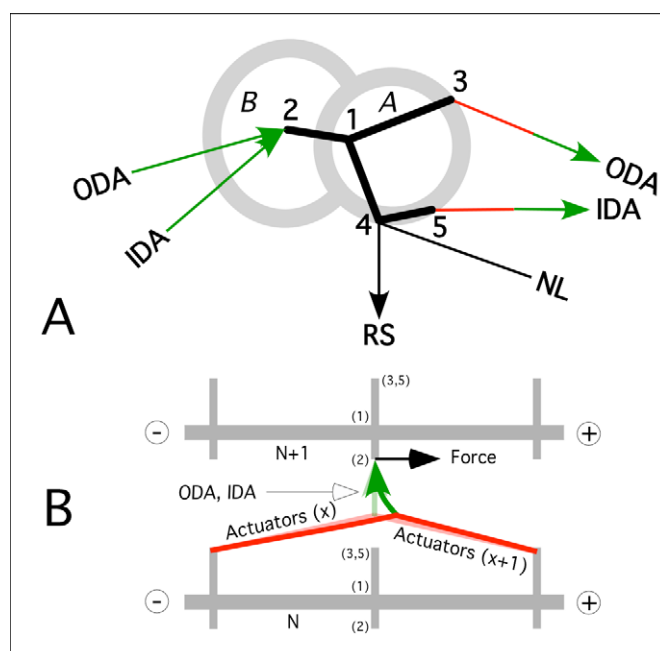
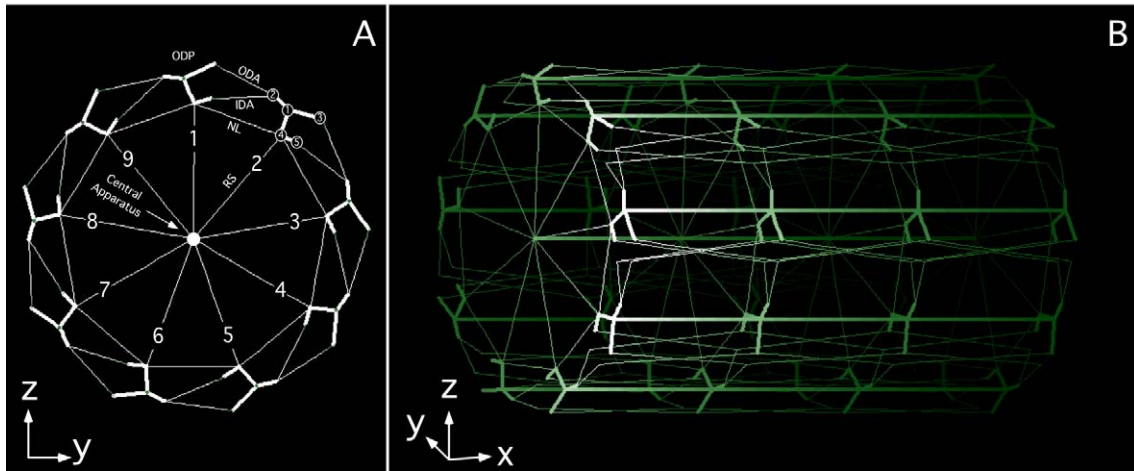


Figure 2



Accepted manuscript

Figure 3

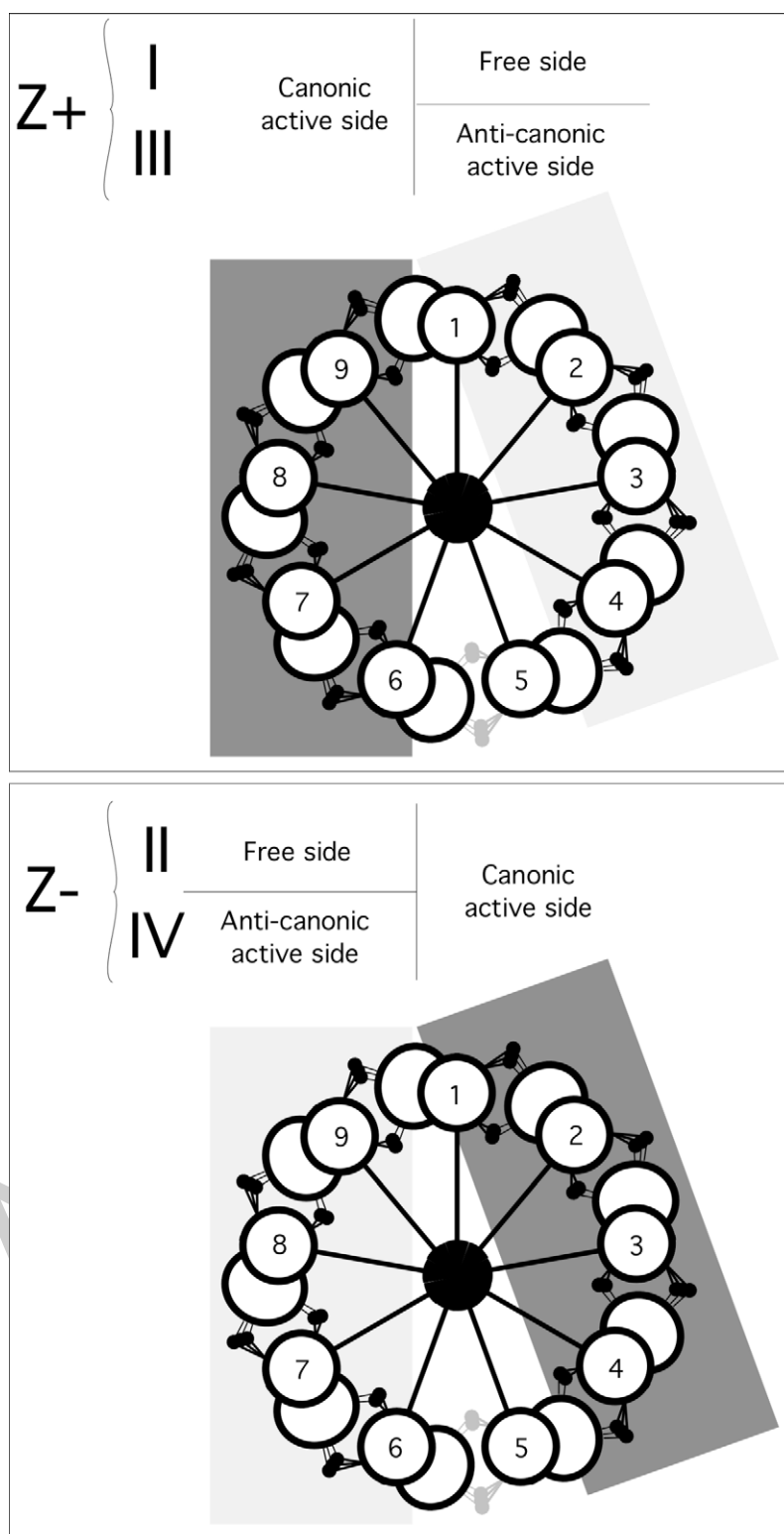


Figure 4

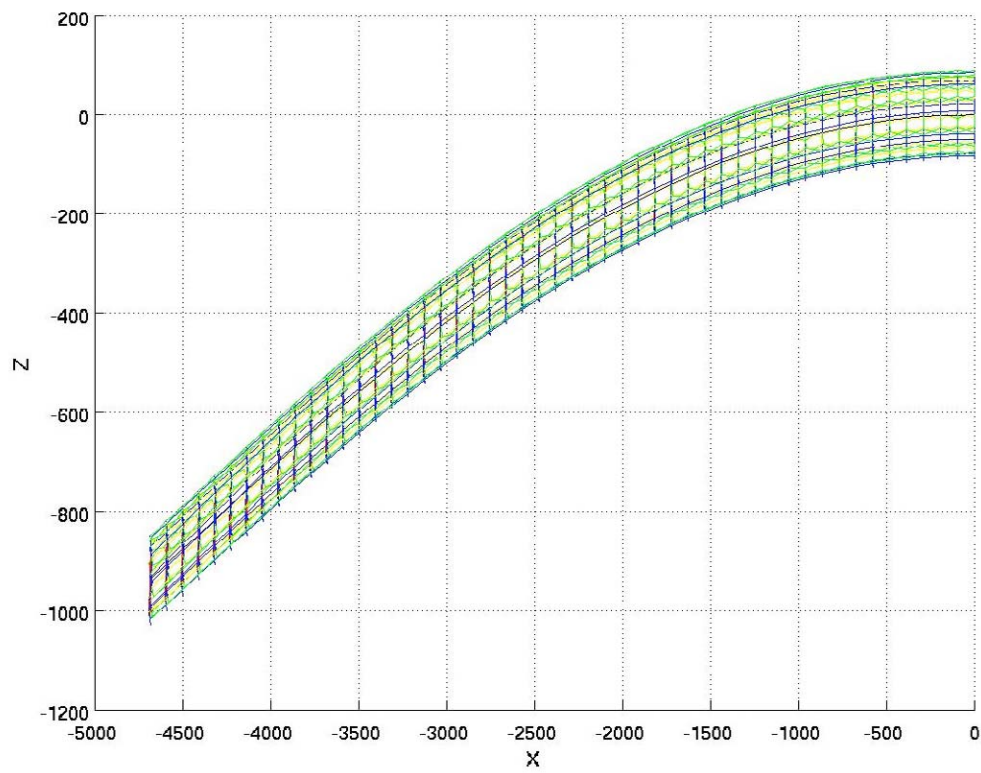


Figure 5

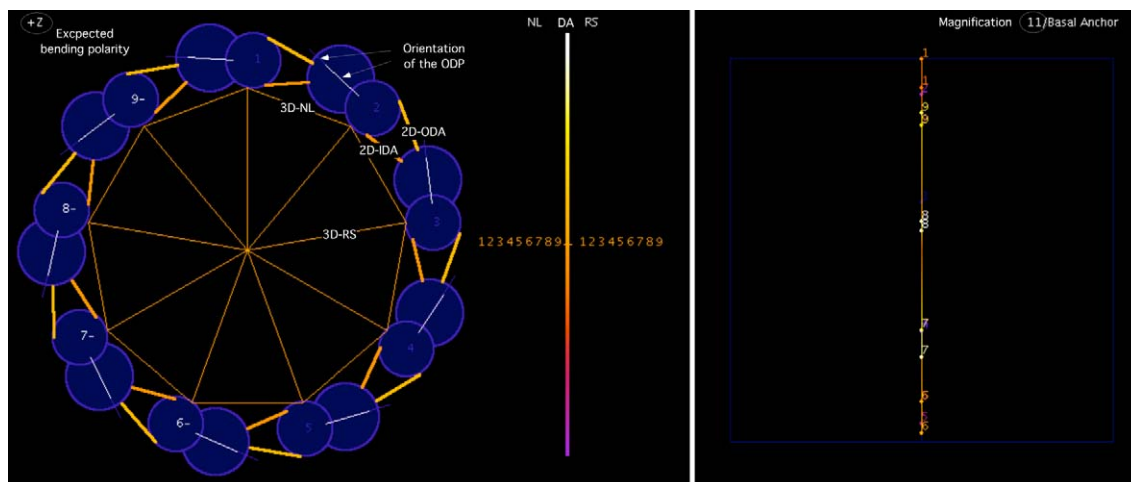


Figure 6

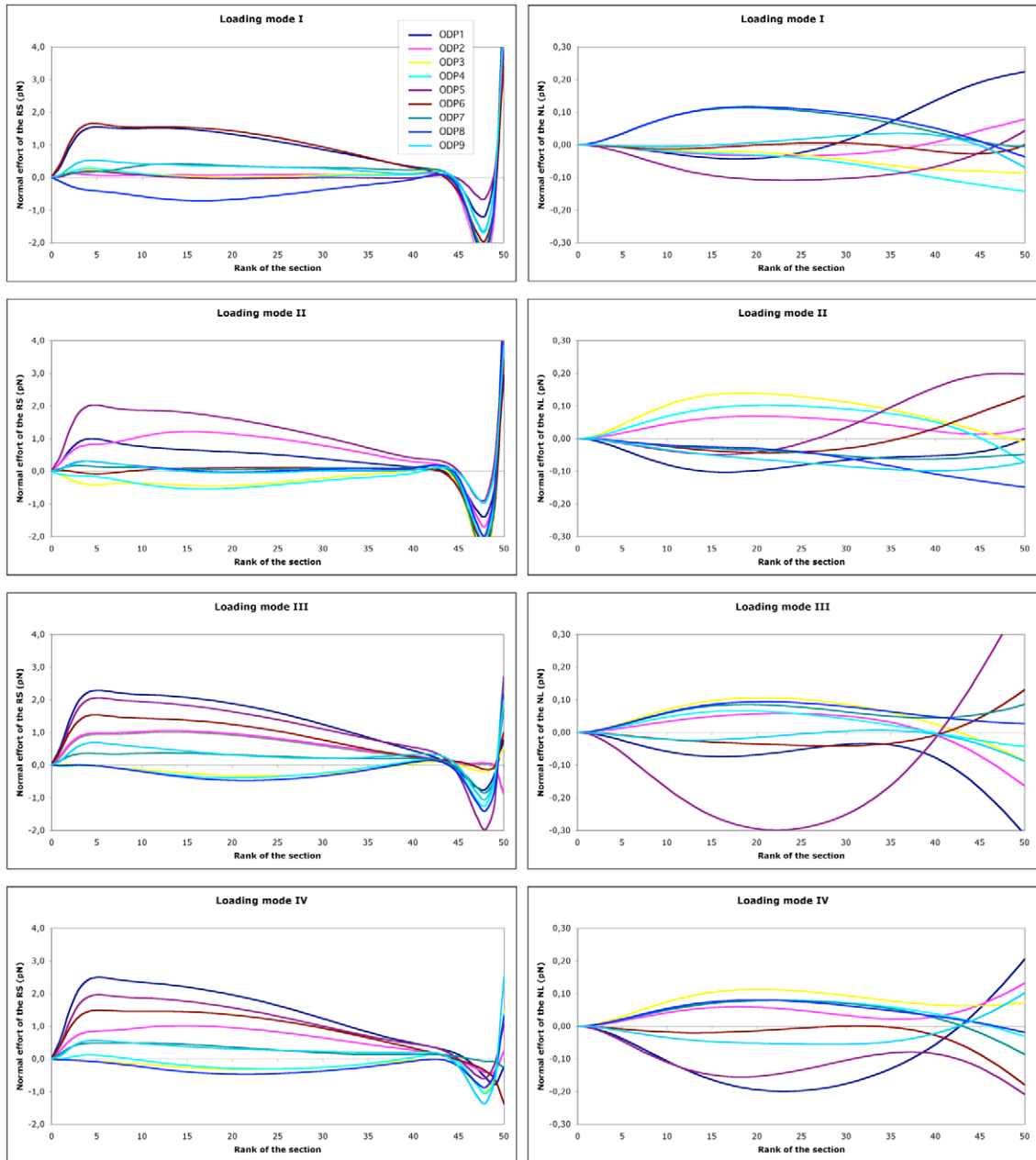


Figure 7

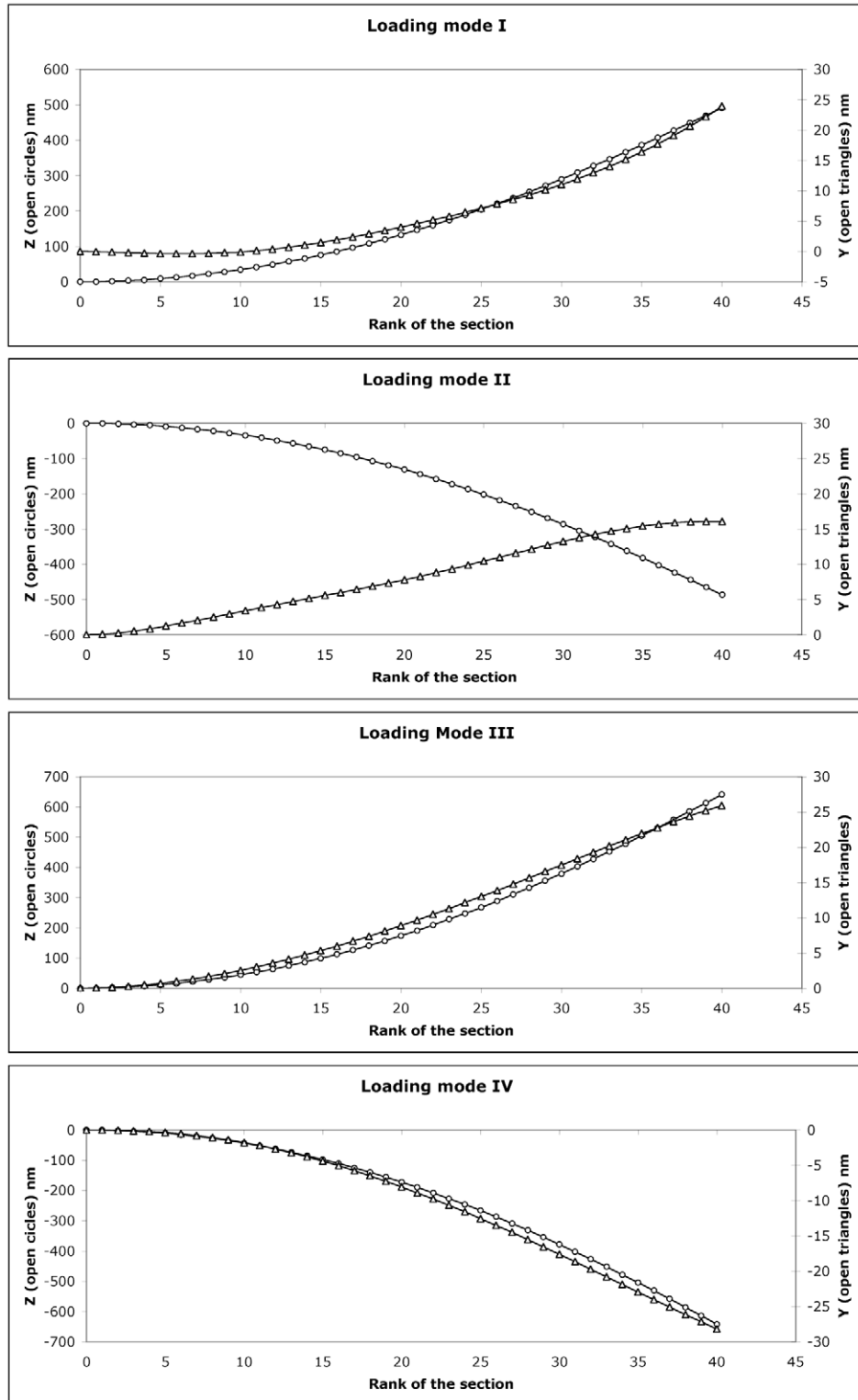
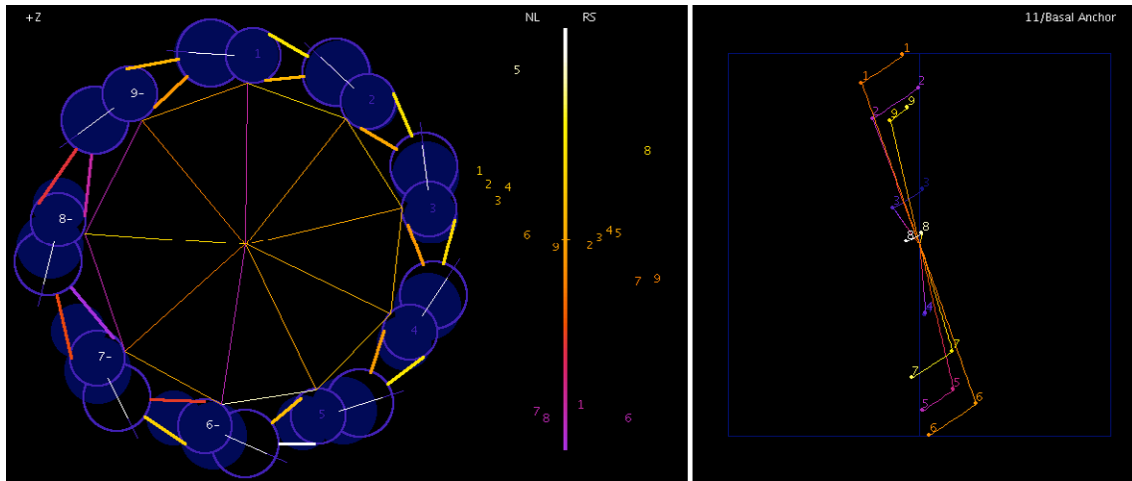


Figure 8

Loading Mode I (section #21)



Loading Mode II (section #21)

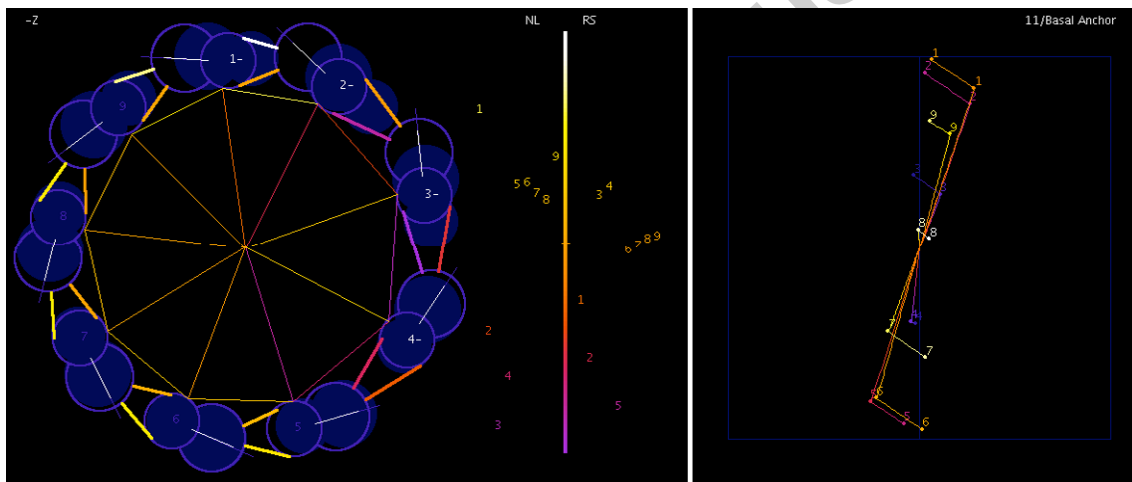
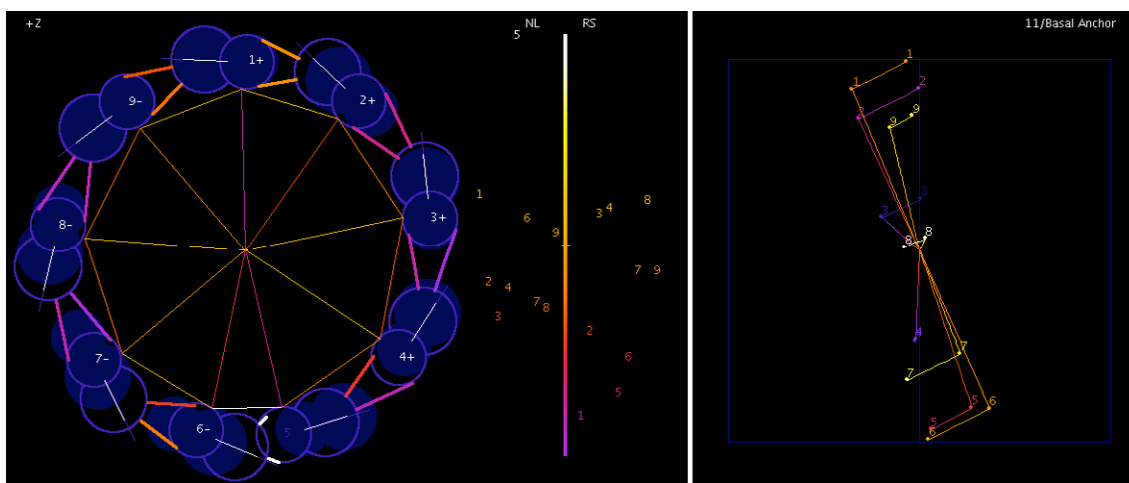


Figure 9

Loading Mode III (section #21)



Loading Mode IV (section #21)

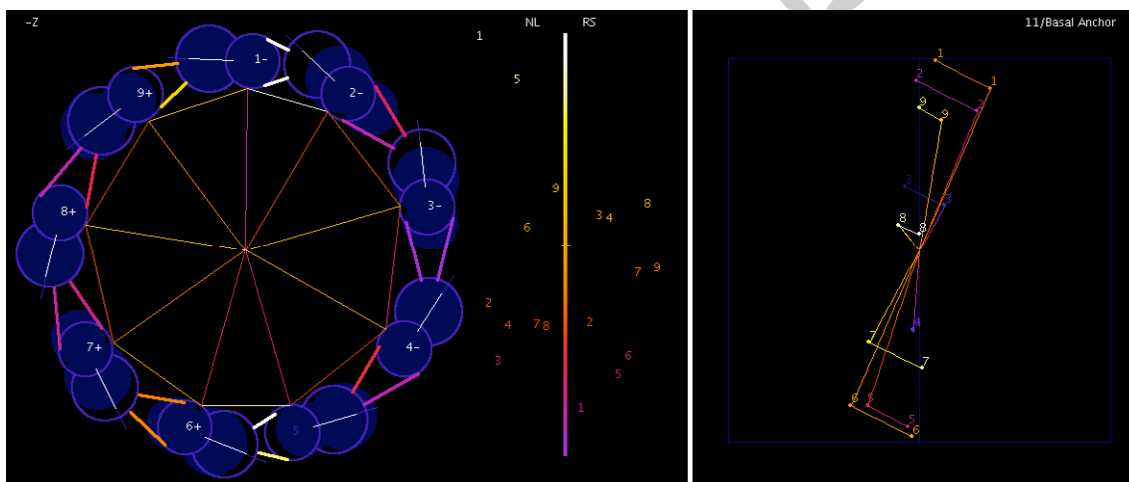
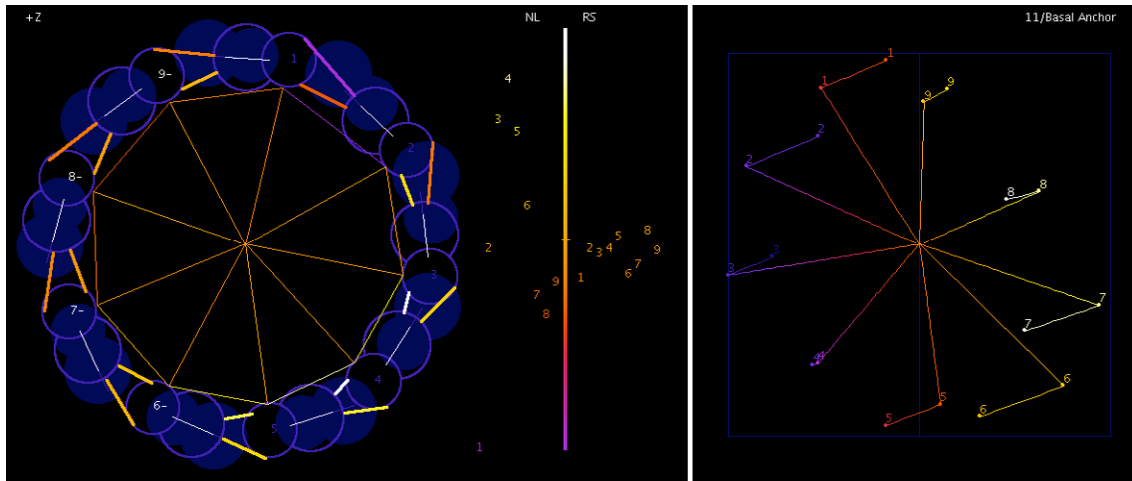


Figure 10

Loading Mode I (section #41)



Loading Mode II (section #41)

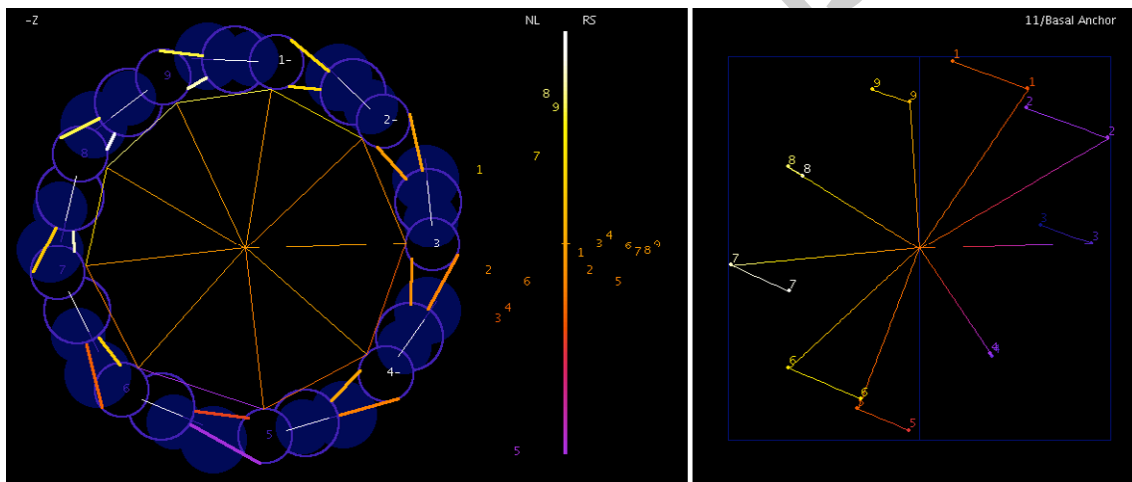
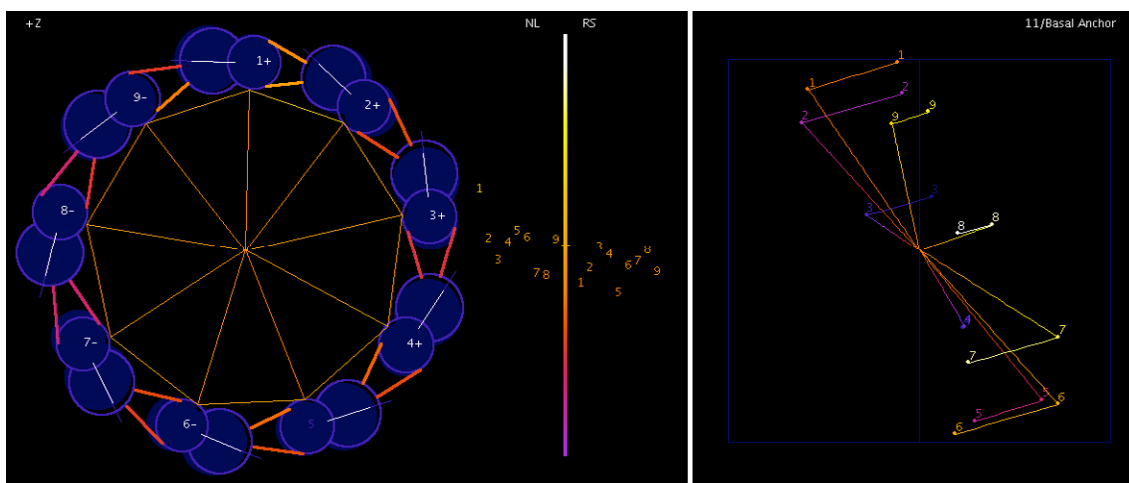


Figure 11

Loading Mode III (section #41)



Loading Mode IV (section #41)

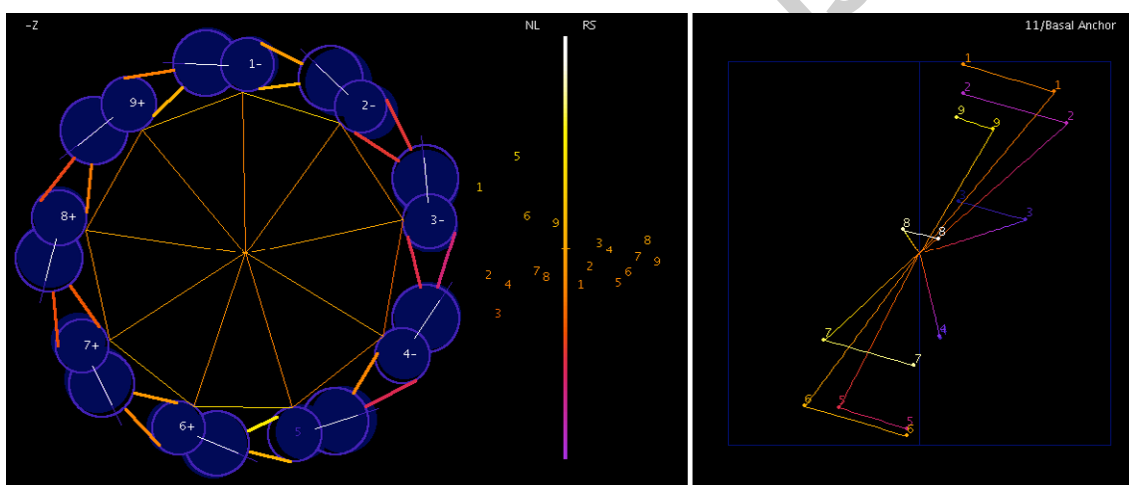


Figure 12

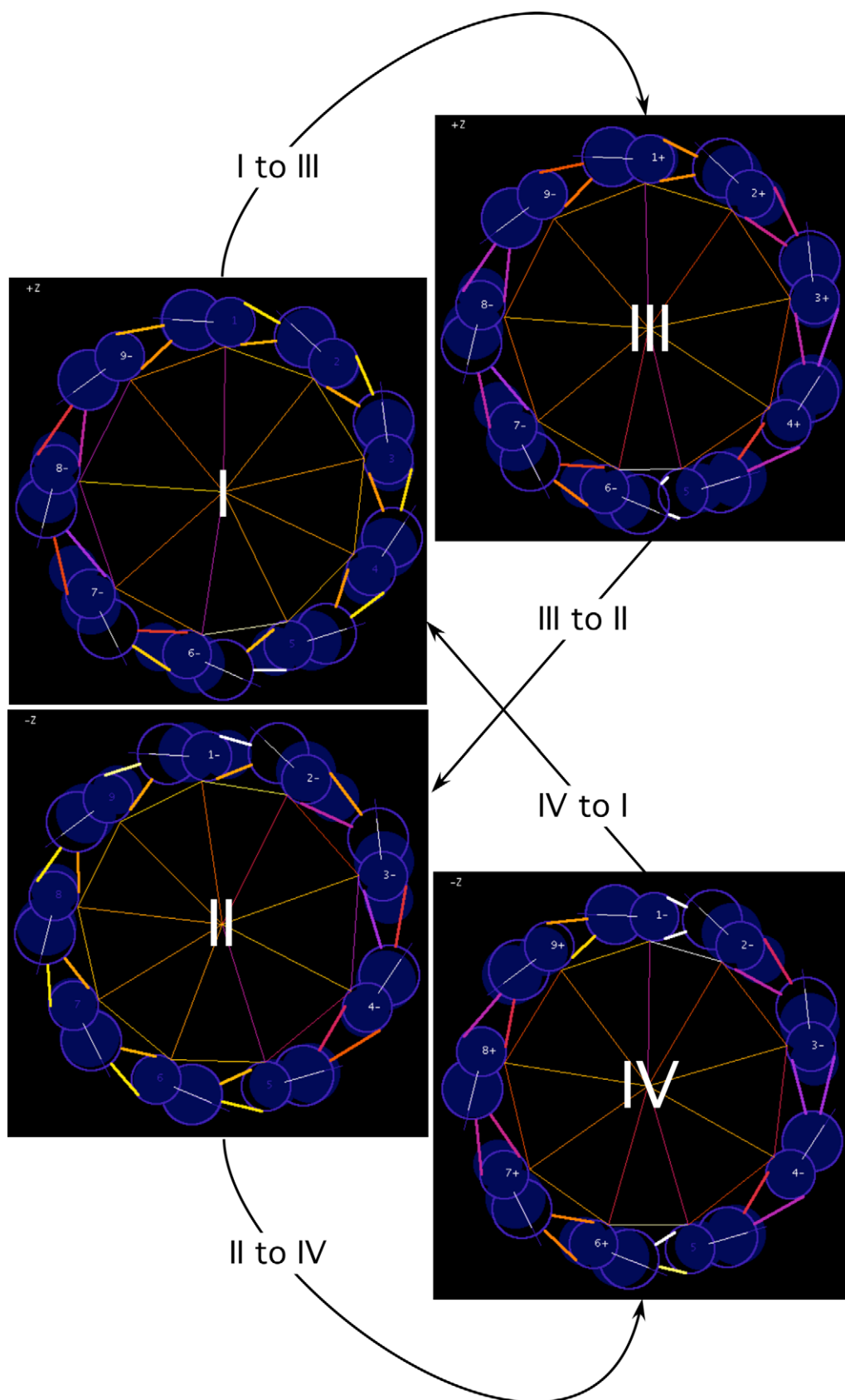


Figure 13

